Chapter 1

Overview of the ATLAS detector

The Large Hadron Collider (LHC) at CERN will extend the frontiers of particle physics with its unprecedented high energy and luminosity. Inside the LHC, bunches of up to 10^{11} protons (p) will collide 40 million times per second to provide 14 TeV proton-proton collisions at a design luminosity of 10^{34} cm^{-2}s^{-1}. The LHC will also collide heavy ions (A), in particular lead nuclei, at 5.5 TeV per nucleon pair, at a design luminosity of 10^{27} cm^{-2}s^{-1}.

The high interaction rates, radiation doses, particle multiplicities and energies, as well as the requirements for precision measurements have set new standards for the design of particle detectors. Two general purpose detectors, ATLAS (A Toroidal LHC ApparatuS) and CMS (Compact Muon Solenoid) have been built for probing p-p and A-A collisions.

This paper presents a comprehensive overview of the ATLAS detector prior to the first LHC collisions, written as the installation of the ATLAS detector is nearing completion. This detector represents the work of a large collaboration of several thousand physicists, engineers, technicians, and students over a period of fifteen years of dedicated design, development, fabrication, and installation.

1.1 Physics requirements and detector overview

The coordinate system and nomenclature used to describe the ATLAS detector and the particles emerging from the p-p collisions are briefly summarised here, since they are used repeatedly throughout this paper. The nominal interaction point is defined as the origin of the coordinate system, while the beam direction defines the z-axis and the x-y plane is transverse to the beam direction. The positive x-axis is defined as pointing from the interaction point to the centre of the LHC ring and the positive y-axis is defined as pointing upwards. The side-A of the detector is defined as that with positive z and side-C is that with negative z. The azimuthal angle ϕ is measured as usual around the beam axis, and the polar angle θ is the angle from the beam axis. The pseudorapidity is defined as $\eta = -\ln\tan(\theta/2)$ (in the case of massive objects such as jets, the rapidity $y = 1/2\ln[(E+p_z)/(E-p_z)]$ is used). The transverse momentum p_T, the transverse energy E_T, and the missing transverse energy E_T^{miss} are defined in the x-y plane unless stated otherwise. The distance ΔR in the pseudorapidity-azimuthal angle space is defined as $\Delta R = \sqrt{\Delta\eta^2 + \Delta\phi^2}$.

The LHC is extensively reviewed in another article of this volume. It will provide a rich physics potential, ranging from more precise measurements of Standard Model parameters to the search for new physics phenomena. Furthermore, nucleus-nucleus collisions at the LHC provide an unprecedented opportunity to study the properties of strongly interacting matter at extreme energy density, including the possible phase transition to a colour-deconfined state: the quark-gluon plasma. Requirements for the ATLAS detector system [1] have been defined using a set of processes covering much of the new phenomena which one can hope to observe at the TeV scale.

The high luminosity and increased cross-sections at the LHC enable further high precision tests of QCD, electroweak interactions, and flavour physics. The top quark will be produced at the LHC at a rate of a few tens of Hz, providing the opportunity to test its couplings and spin.

The search for the Standard Model Higgs boson has been used as a benchmark to establish the performance of important sub-systems of ATLAS. It is a particularly important process since there is a range of production and decay mechanisms, depending on the mass of the Higgs boson, H. At low masses ($m_H < 2m_Z$), the natural width would only be a few MeV, and so the observed width would be defined by the instrumental resolution. The predominant decay mode into hadrons would be difficult to detect due to QCD backgrounds, and the two-photon decay channel would be an important one. Other promising channels could be, for example, associated production of H such as $t\bar{t}H$, WH, and ZH, with $H \rightarrow b\bar{b}$, using a lepton from the decay of one of the top quarks or of the vector boson for triggering and background rejection. For masses above 130 GeV, Higgs-boson decays, $H \rightarrow ZZ^{(*)}$, where each Z decays to a pair of oppositely charged leptons, would provide the experimentally cleanest channel to study the properties of the Higgs boson. For masses above approximately 600 GeV, WW and ZZ decays into jets or involving neutrinos would be needed to extract a signal. The tagging of forward jets from the WW or ZZ fusion production mechanism has also been shown to be important for the discovery of the Higgs boson. Searches for the Higgs boson beyond the Standard Model, for such particles as the A and $H^{\pm}$ of the minimal supersymmetric extension of the Standard Model, require sensitivity to processes involving τ-leptons and good b-tagging performance. Should the Higgs boson be discovered, it would need to be studied in several modes, regardless of its mass, in order to fully disentangle its properties and establish its credentials as belonging to the Standard Model or an extension thereof.

New heavy gauge bosons W' and Z' could be accessible for masses up to ~ 6 TeV. To study their leptonic decays, high-resolution lepton measurements and charge identification are needed in the p_T-range of a few TeV. Another class of signatures of new physics may be provided by very high-p_T jet measurements. As a benchmark process, quark compositeness has been used, where the signature would be a deviation in the jet cross-sections from the QCD expectations. Searches for flavour-changing neutral currents and lepton flavour violation through $\tau \rightarrow 3\mu$ or $\tau \rightarrow \mu\gamma$, as well as measurements of $B_s^0 \rightarrow \mu\mu$ and triple and quartic-gauge couplings may also open a window onto new physics.

The decays of supersymmetric particles, such as squarks and gluinos, would involve cascades which, if R-parity is conserved, always contain a lightest stable supersymmetric particle (LSP). As the LSP would interact very weakly with the detector, the experiment would measure a significant missing transverse energy, E_T^{miss}, in the final state. The rest of the cascade would result in a number of leptons and jets. In schemes where the LSP decays into a photon and a gravitino, an increased number of hard isolated photons is expected.

2008 JINST 3 S08003

Several new models propose the existence of extra dimensions leading to a characteristic energy scale of quantum gravity in the TeV region. In terms of experimental signatures, this could lead to the emission of gravitons which escape into extra dimensions and therefore generate E_T^{miss}, or of Kaluza-Klein excitations which manifest themselves as Z-like resonances with $\sim$ TeV separations in mass. Other experimental signatures could be anomalous high-mass di-jet production, and miniature black-hole production with spectacular decays involving democratic production of fundamental final states such as jets, leptons, photons, neutrinos, W's, and Z's.

The formidable LHC luminosity and resulting interaction rate are needed because of the small cross-sections expected for many of the processes mentioned above. However, with an inelastic-proton-proton cross-section of 80 mb, the LHC will produce a total rate of 10^9 inelastic events/s at design luminosity. This presents a serious experimental difficulty as it implies that every candidate event for new physics will on the average be accompanied by 23 inelastic events per bunch-crossing.

The nature of proton-proton collisions imposes another difficulty. QCD jet production cross-sections dominate over the rare processes mentioned above, requiring the identification of experimental signatures characteristic of the physics processes in question, such as E_T^{miss} or secondary vertices. Identifying such final states for these rare processes imposes further demands on the integrated luminosity needed, and on the particle-identification capabilities of the detector.

Viewed in this context, these benchmark physics goals can be turned into a set of general requirements for the LHC detectors.

- Due to the experimental conditions at the LHC, the detectors require fast, radiation-hard electronics and sensor elements. In addition, high detector granularity is needed to handle the particle fluxes and to reduce the influence of overlapping events.
- Large acceptance in pseudorapidity with almost full azimuthal angle coverage is required.
- Good charged-particle momentum resolution and reconstruction efficiency in the inner tracker are essential. For offline tagging of τ-leptons and b-jets, vertex detectors close to the interaction region are required to observe secondary vertices.
- Very good electromagnetic (EM) calorimetry for electron and photon identification and measurements, complemented by full-coverage hadronic calorimetry for accurate jet and missing transverse energy measurements, are important requirements, as these measurements form the basis of many of the studies mentioned above.
- Good muon identification and momentum resolution over a wide range of momenta and the ability to determine unambiguously the charge of high p_T muons are fundamental requirements.
- Highly efficient triggering on low transverse-momentum objects with sufficient background rejection, is a prerequisite to achieve an acceptable trigger rate for most physics processes of interest.

The overall ATLAS detector layout is shown in figure 1.1 and its main performance goals are listed in table 1.1. It is important to note that, for high-p_T muons, the muon-spectrometer performance as given in table 1.1 is independent of the inner-detector system.

2008 JINST 3 S08003

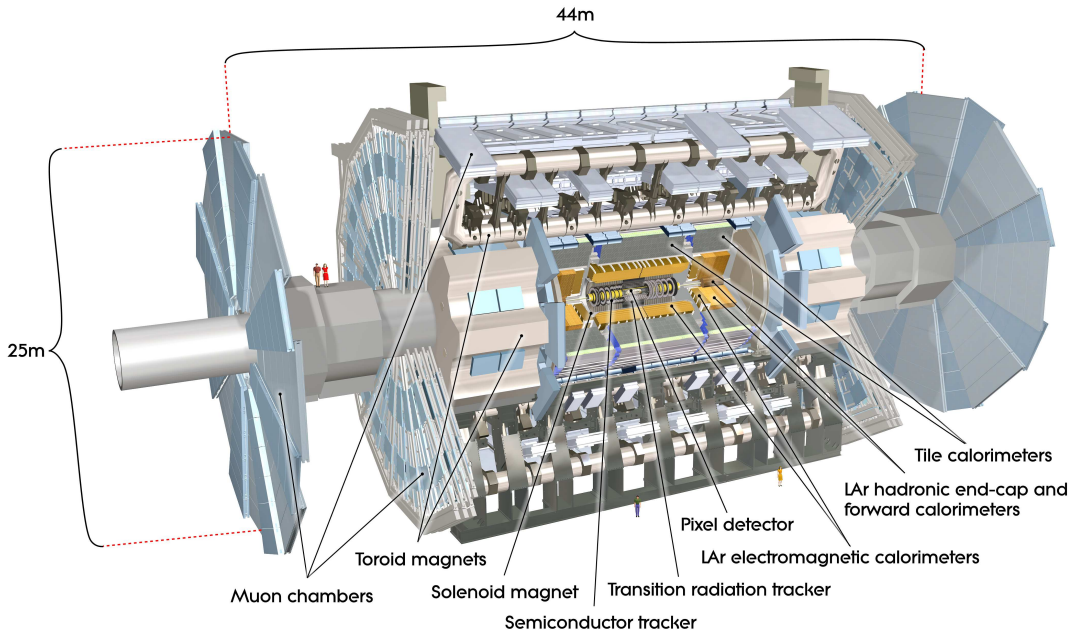

Figure 1.1: Cut-away view of the ATLAS detector. The dimensions of the detector are 25 m in height and 44 m in length. The overall weight of the detector is approximately 7000 tonnes.

The ATLAS detector is nominally forward-backward symmetric with respect to the interaction point. The magnet configuration comprises a thin superconducting solenoid surrounding the inner-detector cavity, and three large superconducting toroids (one barrel and two end-caps) arranged with an eight-fold azimuthal symmetry around the calorimeters. This fundamental choice has driven the design of the rest of the detector.

The inner detector is immersed in a 2 T solenoidal field. Pattern recognition, momentum and vertex measurements, and electron identification are achieved with a combination of discrete, high-resolution semiconductor pixel and strip detectors in the inner part of the tracking volume, and straw-tube tracking detectors with the capability to generate and detect transition radiation in its outer part.

High granularity liquid-argon (LAr) electromagnetic sampling calorimeters, with excellent performance in terms of energy and position resolution, cover the pseudorapidity range $|\eta| < 3.2$. The hadronic calorimetry in the range $|\eta| < 1.7$ is provided by a scintillator-tile calorimeter, which is separated into a large barrel and two smaller extended barrel cylinders, one on either side of the central barrel. In the end-caps ($|\eta| > 1.5$), LAr technology is also used for the hadronic calorimeters, matching the outer $|\eta|$ limits of end-cap electromagnetic calorimeters. The LAr forward calorimeters provide both electromagnetic and hadronic energy measurements, and extend the pseudorapidity coverage to $|\eta| = 4.9$.

The calorimeter is surrounded by the muon spectrometer. The air-core toroid system, with a long barrel and two inserted end-cap magnets, generates strong bending power in a large volume within a light and open structure. Multiple-scattering effects are thereby minimised, and excellent muon momentum resolution is achieved with three layers of high precision tracking chambers.

2008 JINST 3 S08003

Table 1.1: General performance goals of the ATLAS detector. Note that, for high-p_T muons, the muon-spectrometer performance is independent of the inner-detector system. The units for E and p_T are in GeV.

Detector component	**Required resolution**	**η coverage**	
		Measurement	Trigger
Tracking	$\sigma_{p_T}/p_T = 0.05\%\ p_T \oplus 1\%$	± 2.5	
EM calorimetry	$\sigma_E/E = 10\%/\sqrt{E} \oplus 0.7\%$	± 3.2	± 2.5
Hadronic calorimetry (jets)			
barrel and end-cap	$\sigma_E/E = 50\%/\sqrt{E} \oplus 3\%$	± 3.2	± 3.2
forward	$\sigma_E/E = 100\%/\sqrt{E} \oplus 10\%$	$3.1 < \lvert\eta\rvert < 4.9$	$3.1 < \lvert\eta\rvert < 4.9$
Muon spectrometer	σ_{p_T}/p_T=10% at p_T = 1 TeV	± 2.7	± 2.4

The muon instrumentation includes, as a key component, trigger chambers with timing resolution of the order of 1.5-4 ns. The muon spectrometer defines the overall dimensions of the ATLAS detector.

The proton-proton interaction rate at the design luminosity of 10^{34} cm^{-2}s^{-1} is approximately 1 GHz, while the event data recording, based on technology and resource limitations, is limited to about 200 Hz. This requires an overall rejection factor of 5×10^6 against minimum-bias processes while maintaining maximum efficiency for the new physics. The Level-1 (L1) trigger system uses a subset of the total detector information to make a decision on whether or not to continue processing an event, reducing the data rate to approximately 75 kHz (limited by the bandwidth of the readout system, which is upgradeable to 100 kHz). The subsequent two levels, collectively known as the high-level trigger, are the Level-2 (L2) trigger and the event filter. They provide the reduction to a final data-taking rate of approximately 200 Hz.

Due to budgetary constraints, some detector systems had to be staged. They will be completed and installed as soon as technically and financially feasible. These include, in particular, a significant part of the high-level trigger processing farm. The initial input capacity will be limited to a L1 trigger rate of about 40 kHz. This capacity will be increased as needed to deal with the LHC luminosity profile during the first years. The ultimate goal is to be able to handle 100 kHz if needed. Some parts of the muon spectrometer are staged, most noticeably part of the precision chambers in the transition region between the barrel and the end-caps. In addition, some of the forward shielding elements will be completed later, as the LHC approaches design luminosity.

1.2 Tracking

Approximately 1000 particles will emerge from the collision point every 25 ns within $|\eta| < 2.5$, creating a very large track density in the detector. To achieve the momentum and vertex resolution requirements imposed by the benchmark physics processes, high-precision measurements must be made with fine detector granularity. Pixel and silicon microstrip (SCT) trackers, used in conjunction with the straw tubes of the Transition Radiation Tracker (TRT), offer these features.

2008 JINST 3 S08003

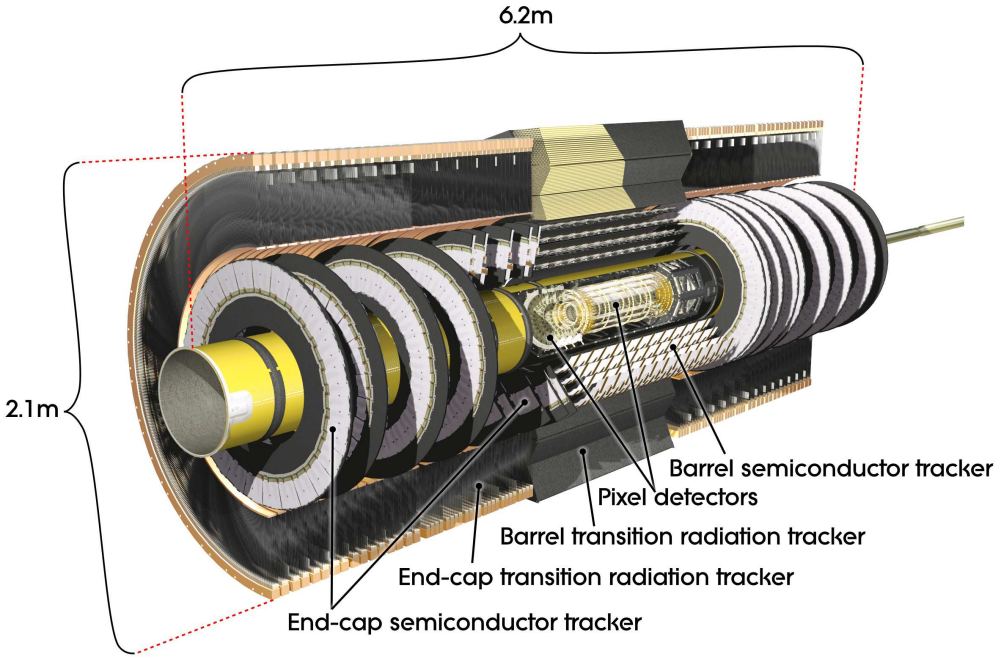

Figure 1.2: Cut-away view of the ATLAS inner detector.

The layout of the Inner Detector (ID) is illustrated in figure 1.2 and detailed in chapter 4. Its basic parameters are summarised in table 1.2 (also see intrinsic accuracies in table 4.1). The ID is immersed in a 2 T magnetic field generated by the central solenoid, which extends over a length of 5.3 m with a diameter of 2.5 m. The precision tracking detectors (pixels and SCT) cover the region $|\eta| < 2.5$. In the barrel region, they are arranged on concentric cylinders around the beam axis while in the end-cap regions they are located on disks perpendicular to the beam axis. The highest granularity is achieved around the vertex region using silicon pixel detectors. The pixel layers are segmented in $R-\phi$ and z with typically three pixel layers crossed by each track. All pixel sensors are identical and have a minimum pixel size in $R-\phi \times z$ of 50×400 μm^2. The intrinsic accuracies in the barrel are 10 μm ($R-\phi$) and 115 μm (z) and in the disks are 10 μm ($R-\phi$) and 115 μm (R). The pixel detector has approximately 80.4 million readout channels. For the SCT, eight strip layers (four space points) are crossed by each track. In the barrel region, this detector uses small-angle (40 mrad) stereo strips to measure both coordinates, with one set of strips in each layer parallel to the beam direction, measuring $R-\phi$. They consist of two 6.4 cm long daisy-chained sensors with a strip pitch of 80 μm. In the end-cap region, the detectors have a set of strips running radially and a set of stereo strips at an angle of 40 mrad. The mean pitch of the strips is also approximately 80 μm. The intrinsic accuracies per module in the barrel are 17 μm ($R-\phi$) and 580 μm (z) and in the disks are 17 μm ($R-\phi$) and 580 μm (R). The total number of readout channels in the SCT is approximately 6.3 million.

A large number of hits (typically 36 per track) is provided by the 4 mm diameter straw tubes of the TRT, which enables track-following up to $|\eta| = 2.0$. The TRT only provides $R-\phi$ information, for which it has an intrinsic accuracy of 130 μm per straw. In the barrel region, the straws are parallel to the beam axis and are 144 cm long, with their wires divided into two halves, approximately at $\eta = 0$. In the end-cap region, the 37 cm long straws are arranged radially in wheels. The total number of TRT readout channels is approximately 351,000.

Table 1.2: Main parameters of the inner-detector system.

Item		**Radial extension (mm)**	**Length (mm)**
Overall ID envelope		$0 < R < 1150$	$0 < \|z\| < 3512$
Beam-pipe		$29 < R < 36$	
Pixel	Overall envelope	$45.5 < R < 242$	$0 < \|z\| < 3092$
3 cylindrical layers	Sensitive barrel	$50.5 < R < 122.5$	$0 < \|z\| < 400.5$
2×3 disks	Sensitive end-cap	$88.8 < R < 149.6$	$495 < \|z\| < 650$
SCT	Overall envelope	$255 < R < 549$ (barrel)	$0 < \|z\| < 805$
		$251 < R < 610$ (end-cap)	$810 < \|z\| < 2797$
4 cylindrical layers	Sensitive barrel	$299 < R < 514$	$0 < \|z\| < 749$
2×9 disks	Sensitive end-cap	$275 < R < 560$	$839 < \|z\| < 2735$
TRT	Overall envelope	$554 < R < 1082$ (barrel)	$0 < \|z\| < 780$
		$617 < R < 1106$ (end-cap)	$827 < \|z\| < 2744$
73 straw planes	Sensitive barrel	$563 < R < 1066$	$0 < \|z\| < 712$
160 straw planes	Sensitive end-cap	$644 < R < 1004$	$848 < \|z\| < 2710$

The combination of precision trackers at small radii with the TRT at a larger radius gives very robust pattern recognition and high precision in both $R-\phi$ and z coordinates. The straw hits at the outer radius contribute significantly to the momentum measurement, since the lower precision per point compared to the silicon is compensated by the large number of measurements and longer measured track length.

The inner detector system provides tracking measurements in a range matched by the precision measurements of the electromagnetic calorimeter. The electron identification capabilities are enhanced by the detection of transition-radiation photons in the xenon-based gas mixture of the straw tubes. The semiconductor trackers also allow impact parameter measurements and vertexing for heavy-flavour and τ-lepton tagging. The secondary vertex measurement performance is enhanced by the innermost layer of pixels, at a radius of about 5 cm.

1.3 Calorimetry

A view of the sampling calorimeters is presented in figure 1.3, and the pseudorapidity coverage, granularity, and segmentation in depth of the calorimeters are summarised in table 1.3 (see also chapter 5). These calorimeters cover the range $|\eta| < 4.9$, using different techniques suited to the widely varying requirements of the physics processes of interest and of the radiation environment over this large η-range. Over the η region matched to the inner detector, the fine granularity of the EM calorimeter is ideally suited for precision measurements of electrons and photons. The coarser granularity of the rest of the calorimeter is sufficient to satisfy the physics requirements for jet reconstruction and E_T^{miss} measurements.

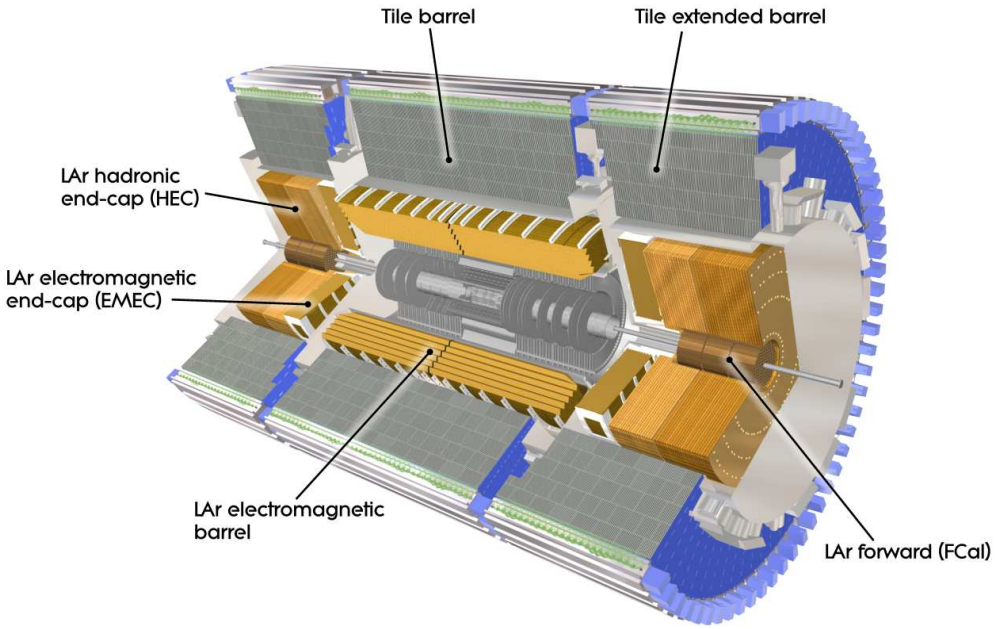

Figure 1.3: Cut-away view of the ATLAS calorimeter system.

Calorimeters must provide good containment for electromagnetic and hadronic showers, and must also limit punch-through into the muon system. Hence, calorimeter depth is an important design consideration. The total thickness of the EM calorimeter is > 22 radiation lengths (X_0) in the barrel and > 24 X_0 in the end-caps. The approximate 9.7 interaction lengths (λ) of active calorimeter in the barrel (10 λ in the end-caps) are adequate to provide good resolution for high-energy jets (see table 1.1). The total thickness, including 1.3 λ from the outer support, is 11 λ at $\eta = 0$ and has been shown both by measurements and simulations to be sufficient to reduce punch-through well below the irreducible level of prompt or decay muons. Together with the large η-coverage, this thickness will also ensure a good E_T^{miss} measurement, which is important for many physics signatures and in particular for SUSY particle searches.

1.3.1 LAr electromagnetic calorimeter

The EM calorimeter is divided into a barrel part ($|\eta| < 1.475$) and two end-cap components ($1.375 < |\eta| < 3.2$), each housed in their own cryostat. The position of the central solenoid in front of the EM calorimeter demands optimisation of the material in order to achieve the desired calorimeter performance. As a consequence, the central solenoid and the LAr calorimeter share a common vacuum vessel, thereby eliminating two vacuum walls. The barrel calorimeter consists of two identical half-barrels, separated by a small gap (4 mm) at $z = 0$. Each end-cap calorimeter is mechanically divided into two coaxial wheels: an outer wheel covering the region $1.375 < |\eta| < 2.5$, and an inner wheel covering the region $2.5 < |\eta| < 3.2$. The EM calorimeter is a lead-LAr detector with accordion-shaped kapton electrodes and lead absorber plates over its full coverage. The accordion geometry provides complete ϕ symmetry without azimuthal cracks. The

2008 JINST 3 S08003

Table 1.3: Main parameters of the calorimeter system.

	Barrel		End-cap	
EM calorimeter				
Number of layers and $\|\eta\|$ coverage				
Presampler	1	$\|\eta\| < 1.52$	1	$1.5 < \|\eta\| < 1.8$
Calorimeter	3	$\|\eta\| < 1.35$	2	$1.375 < \|\eta\| < 1.5$
	2	$1.35 < \|\eta\| < 1.475$	3	$1.5 < \|\eta\| < 2.5$
			2	$2.5 < \|\eta\| < 3.2$
Granularity $\Delta\eta \times \Delta\phi$ versus $\|\eta\|$				
Presampler	0.025×0.1	$\|\eta\| < 1.52$	0.025×0.1	$1.5 < \|\eta\| < 1.8$
Calorimeter 1st layer	$0.025/8 \times 0.1$	$\|\eta\| < 1.40$	0.050×0.1	$1.375 < \|\eta\| < 1.425$
	0.025×0.025	$1.40 < \|\eta\| < 1.475$	0.025×0.1	$1.425 < \|\eta\| < 1.5$
			$0.025/8 \times 0.1$	$1.5 < \|\eta\| < 1.8$
			$0.025/6 \times 0.1$	$1.8 < \|\eta\| < 2.0$
			$0.025/4 \times 0.1$	$2.0 < \|\eta\| < 2.4$
			0.025×0.1	$2.4 < \|\eta\| < 2.5$
			0.1×0.1	$2.5 < \|\eta\| < 3.2$
Calorimeter 2nd layer	0.025×0.025	$\|\eta\| < 1.40$	0.050×0.025	$1.375 < \|\eta\| < 1.425$
	0.075×0.025	$1.40 < \|\eta\| < 1.475$	0.025×0.025	$1.425 < \|\eta\| < 2.5$
			0.1×0.1	$2.5 < \|\eta\| < 3.2$
Calorimeter 3rd layer	0.050×0.025	$\|\eta\| < 1.35$	0.050×0.025	$1.5 < \|\eta\| < 2.5$
Number of readout channels				
Presampler	7808		1536 (both sides)	
Calorimeter	101760		62208 (both sides)	
LAr hadronic end-cap				
$\|\eta\|$ coverage			$1.5 < \|\eta\| < 3.2$	
Number of layers			4	
Granularity $\Delta\eta \times \Delta\phi$			0.1×0.1	$1.5 < \|\eta\| < 2.5$
			0.2×0.2	$2.5 < \|\eta\| < 3.2$
Readout channels			5632 (both sides)	
LAr forward calorimeter				
$\|\eta\|$ coverage			$3.1 < \|\eta\| < 4.9$	
Number of layers			3	
Granularity $\Delta x \times \Delta y$ (cm)			FCal1: 3.0×2.6	$3.15 < \|\eta\| < 4.30$
			FCal1: $\sim$ four times finer	$3.10 < \|\eta\| < 3.15$,
				$4.30 < \|\eta\| < 4.83$
			FCal2: 3.3×4.2	$3.24 < \|\eta\| < 4.50$
			FCal2: $\sim$ four times finer	$3.20 < \|\eta\| < 3.24$,
				$4.50 < \|\eta\| < 4.81$
			FCal3: 5.4×4.7	$3.32 < \|\eta\| < 4.60$
			FCal3: $\sim$ four times finer	$3.29 < \|\eta\| < 3.32$,
				$4.60 < \|\eta\| < 4.75$
Readout channels			3524 (both sides)	
Scintillator tile calorimeter				
	Barrel		Extended barrel	
$\|\eta\|$ coverage	$\|\eta\| < 1.0$		$0.8 < \|\eta\| < 1.7$	
Number of layers	3		3	
Granularity $\Delta\eta \times \Delta\phi$	0.1×0.1		0.1×0.1	
Last layer	0.2×0.1		0.2×0.1	
Readout channels	5760		4092 (both sides)	

lead thickness in the absorber plates has been optimised as a function of η in terms of EM calorimeter performance in energy resolution. Over the region devoted to precision physics ($|\eta| < 2.5$), the EM calorimeter is segmented in three sections in depth. For the end-cap inner wheel, the calorimeter is segmented in two sections in depth and has a coarser lateral granularity than for the rest of the acceptance.

2008 JINST 3 S08003

In the region of $|\eta| < 1.8$, a presampler detector is used to correct for the energy lost by electrons and photons upstream of the calorimeter. The presampler consists of an active LAr layer of thickness 1.1 cm (0.5 cm) in the barrel (end-cap) region.

1.3.2 Hadronic calorimeters

Tile calorimeter. The tile calorimeter is placed directly outside the EM calorimeter envelope. Its barrel covers the region $|\eta| < 1.0$, and its two extended barrels the range $0.8 < |\eta| < 1.7$. It is a sampling calorimeter using steel as the absorber and scintillating tiles as the active material. The barrel and extended barrels are divided azimuthally into 64 modules. Radially, the tile calorimeter extends from an inner radius of 2.28 m to an outer radius of 4.25 m. It is segmented in depth in three layers, approximately 1.5, 4.1 and 1.8 interaction lengths (λ) thick for the barrel and 1.5, 2.6, and 3.3 λ for the extended barrel. The total detector thickness at the outer edge of the tile-instrumented region is 9.7 λ at $\eta = 0$. Two sides of the scintillating tiles are read out by wavelength shifting fibres into two separate photomultiplier tubes. In η, the readout cells built by grouping fibres into the photomultipliers are pseudo-projective towards the interaction region.

LAr hadronic end-cap calorimeter. The Hadronic End-cap Calorimeter (HEC) consists of two independent wheels per end-cap, located directly behind the end-cap electromagnetic calorimeter and sharing the same LAr cryostats. To reduce the drop in material density at the transition between the end-cap and the forward calorimeter (around $|\eta| = 3.1$), the HEC extends out to $|\eta| = 3.2$, thereby overlapping with the forward calorimeter. Similarly, the HEC η range also slightly overlaps that of the tile calorimeter ($|\eta| < 1.7$) by extending to $|\eta| = 1.5$. Each wheel is built from 32 identical wedge-shaped modules, assembled with fixtures at the periphery and at the central bore. Each wheel is divided into two segments in depth, for a total of four layers per end-cap. The wheels closest to the interaction point are built from 25 mm parallel copper plates, while those further away use 50 mm copper plates (for all wheels the first plate is half-thickness). The outer radius of the copper plates is 2.03 m, while the inner radius is 0.475 m (except in the overlap region with the forward calorimeter where this radius becomes 0.372 m). The copper plates are interleaved with 8.5 mm LAr gaps, providing the active medium for this sampling calorimeter.

LAr forward calorimeter. The Forward Calorimeter (FCal) is integrated into the end-cap cryostats, as this provides clear benefits in terms of uniformity of the calorimetric coverage as well as reduced radiation background levels in the muon spectrometer. In order to reduce the amount of neutron albedo in the inner detector cavity, the front face of the FCal is recessed by about 1.2 m with respect to the EM calorimeter front face. This severely limits the depth of the calorimeter and therefore calls for a high-density design. The FCal is approximately 10 interaction lengths deep, and consists of three modules in each end-cap: the first, made of copper, is optimised for electromagnetic measurements, while the other two, made of tungsten, measure predominantly the energy of hadronic interactions. Each module consists of a metal matrix, with regularly spaced longitudinal channels filled with the electrode structure consisting of concentric rods and tubes parallel to the beam axis. The LAr in the gap between the rod and the tube is the sensitive medium. This geometry allows for excellent control of the gaps, which are as small as 0.25 mm in the first section, in order to avoid problems due to ion buildup.

2008 JINST 3 S08003

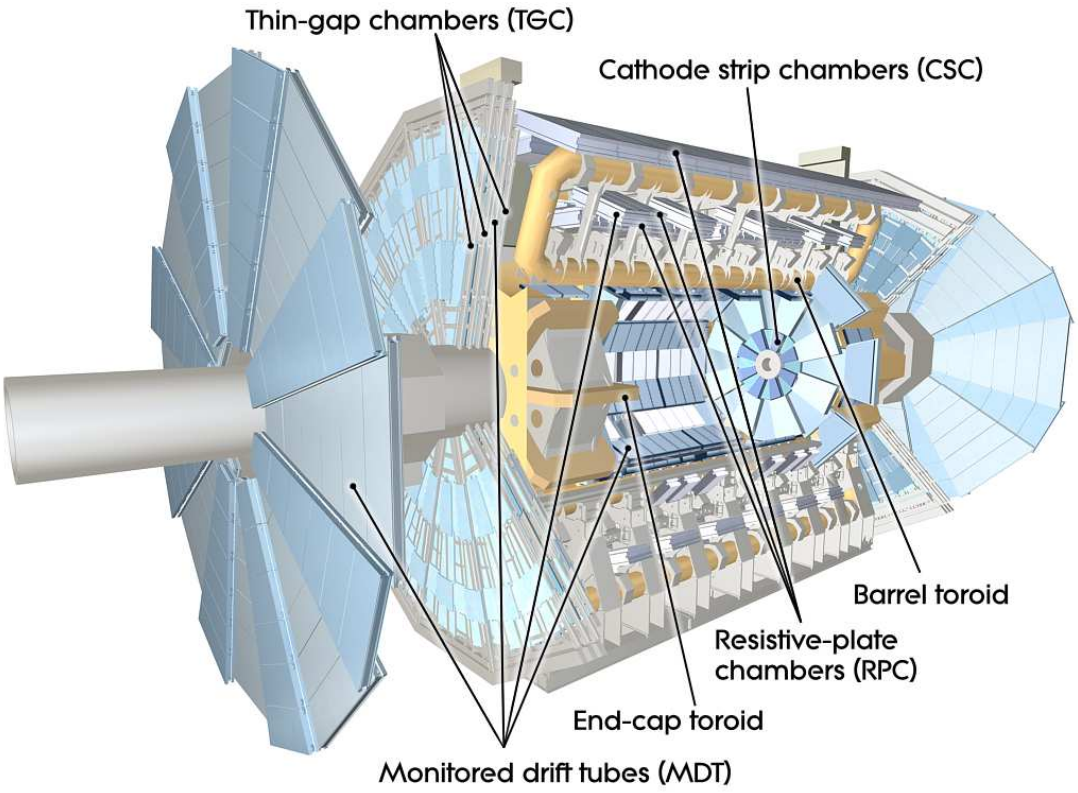

Figure 1.4: Cut-away view of the ATLAS muon system.

1.4 Muon system

The conceptual layout of the muon spectrometer is shown in figure 1.4 and the main parameters of the muon chambers are listed in table 1.4 (see also chapter 6). It is based on the magnetic deflection of muon tracks in the large superconducting air-core toroid magnets, instrumented with separate trigger and high-precision tracking chambers. Over the range $|\eta| < 1.4$, magnetic bending is provided by the large barrel toroid. For $1.6 < |\eta| < 2.7$, muon tracks are bent by two smaller end-cap magnets inserted into both ends of the barrel toroid. Over $1.4 < |\eta| < 1.6$, usually referred to as the transition region, magnetic deflection is provided by a combination of barrel and end-cap fields. This magnet configuration provides a field which is mostly orthogonal to the muon trajectories, while minimising the degradation of resolution due to multiple scattering. The anticipated high level of particle flux has had a major impact on the choice and design of the spectrometer instrumentation, affecting performance parameters such as rate capability, granularity, ageing properties, and radiation hardness.

In the barrel region, tracks are measured in chambers arranged in three cylindrical layers around the beam axis; in the transition and end-cap regions, the chambers are installed in planes perpendicular to the beam, also in three layers.

2008 JINST 3 S08003

Table 1.4: Main parameters of the muon spectrometer. Numbers in brackets for the MDT's and the RPC's refer to the final configuration of the detector in 2009.

Monitored drift tubes	**MDT**
- Coverage	$\|\eta\| < 2.7$ (innermost layer: $\|\eta\| < 2.0$)
- Number of chambers	1088 (1150)
- Number of channels	339 000 (354 000)
- Function	Precision tracking
Cathode strip chambers	**CSC**
- Coverage	$2.0 < \|\eta\| < 2.7$
- Number of chambers	32
- Number of channels	31 000
- Function	Precision tracking
Resistive plate chambers	**RPC**
- Coverage	$\|\eta\| < 1.05$
- Number of chambers	544 (606)
- Number of channels	359 000 (373 000)
- Function	Triggering, second coordinate
Thin gap chambers	**TGC**
- Coverage	$1.05 < \|\eta\| < 2.7$ (2.4 for triggering)
- Number of chambers	3588
- Number of channels	318 000
- Function	Triggering, second coordinate

1.4.1 The toroid magnets

A system of three large air-core toroids generates the magnetic field for the muon spectrometer. The two end-cap toroids are inserted in the barrel toroid at each end and line up with the central solenoid. Each of the three toroids consists of eight coils assembled radially and symmetrically around the beam axis. The end-cap toroid coil system is rotated by 22.5° with respect to the barrel toroid coil system in order to provide radial overlap and to optimise the bending power at the interface between the two coil systems.

The barrel toroid coils are housed in eight individual cryostats, with the linking elements between them providing the overall mechanical stability. Each end-cap toroid consists of eight racetrack-like coils in an aluminium alloy housing. Each coil has two double-pancake type windings. They are cold-linked and assembled as a single cold mass, housed in one large cryostat. Therefore the internal forces in the end-cap toroids are taken by the cold supporting structure between the coils, a different design solution than in the barrel toroid.

The performance in terms of bending power is characterised by the field integral $\int$Bdl, where B is the field component normal to the muon direction and the integral is computed along an infinite-momentum muon trajectory, between the innermost and outermost muon-chamber planes. The barrel toroid provides 1.5 to 5.5 Tm of bending power in the pseudorapidity range $0 < |\eta| < 1.4$, and the end-cap toroids approximately 1 to 7.5 Tm in the region $1.6 < |\eta| < 2.7$. The bending power is lower in the transition regions where the two magnets overlap ($1.4 < |\eta| < 1.6$).

1.4.2 Muon chamber types

Over most of the η-range, a precision measurement of the track coordinates in the principal bending direction of the magnetic field is provided by Monitored Drift Tubes (MDT's). The mechanical isolation in the drift tubes of each sense wire from its neighbours guarantees a robust and reliable operation. At large pseudorapidities, Cathode Strip Chambers (CSC's, which are multiwire proportional chambers with cathodes segmented into strips) with higher granularity are used in the innermost plane over $2 < |\eta| < 2.7$, to withstand the demanding rate and background conditions. The stringent requirements on the relative alignment of the muon chamber layers are met by the combination of precision mechanical-assembly techniques and optical alignment systems both within and between muon chambers.

The trigger system covers the pseudorapidity range $|\eta| < 2.4$. Resistive Plate Chambers (RPC's) are used in the barrel and Thin Gap Chambers (TGC's) in the end-cap regions. The trigger chambers for the muon spectrometer serve a threefold purpose: provide bunch-crossing identification, provide well-defined p_T thresholds, and measure the muon coordinate in the direction orthogonal to that determined by the precision-tracking chambers.

1.4.3 Muon chamber alignment and B-field reconstruction

The overall performance over the large areas involved, particularly at the highest momenta, depends on the alignment of the muon chambers with respect to each other and with respect to the overall detector.

The accuracy of the stand-alone muon momentum measurement necessitates a precision of 30 μm on the relative alignment of chambers both within each projective tower and between consecutive layers in immediately adjacent towers. The internal deformations and relative positions of the MDT chambers are monitored by approximately 12000 precision-mounted alignment sensors, all based on the optical monitoring of deviations from straight lines. Because of geometrical constraints, the reconstruction and/or monitoring of the chamber positions rely on somewhat different strategies and sensor types in the end-cap and barrel regions, respectively.

The accuracy required for the relative positioning of non-adjacent towers to obtain adequate mass resolution for multi-muon final states, lies in the few millimetre range. This initial positioning accuracy is approximately established during the installation of the chambers. Ultimately, the relative alignment of the barrel and forward regions of the muon spectrometer, of the calorimeters and of the inner detector will rely on high-momentum muon trajectories.

For magnetic field reconstruction, the goal is to determine the bending power along the muon trajectory to a few parts in a thousand. The field is continuously monitored by a total of approximately 1800 Hall sensors distributed throughout the spectrometer volume. Their readings are compared with magnetic-field simulations and used for reconstructing the position of the toroid coils in space, as well as to account for magnetic perturbations induced by the tile calorimeter and other nearby metallic structures.

2008 JINST 3 S08003

1.5 Forward detectors

Three smaller detector systems cover the ATLAS forward region (see chapter 7). The main function of the first two systems is to determine the luminosity delivered to ATLAS. At ± 17 m from the interaction point lies LUCID (LUminosity measurement using Cerenkov Integrating Detector). It detects inelastic p-p scattering in the forward direction, and is the main online relative-luminosity monitor for ATLAS. The second detector is ALFA (Absolute Luminosity For ATLAS). Located at ± 240 m, it consists of scintillating fibre trackers located inside Roman pots which are designed to approach as close as 1 mm to the beam. The third system is the Zero-Degree Calorimeter (ZDC), which plays a key role in determining the centrality of heavy-ion collisions. It is located at ± 140 m from the interaction point, just beyond the point where the common straight-section vacuum-pipe divides back into two independent beam-pipes. The ZDC modules consist of layers of alternating quartz rods and tungsten plates which will measure neutral particles at pseudorapidities $|\eta| \geq 8.2$.

1.6 Trigger, readout, data acquisition, and control systems

The Trigger and Data Acquisition (collectively TDAQ) systems, the timing- and trigger-control logic, and the Detector Control System (DCS) are partitioned into sub-systems, typically associated with sub-detectors, which have the same logical components and building blocks (see chapter 8).

The trigger system has three distinct levels: L1, L2, and the event filter. Each trigger level refines the decisions made at the previous level and, where necessary, applies additional selection criteria. The data acquisition system receives and buffers the event data from the detector-specific readout electronics, at the L1 trigger accept rate, over 1600 point-to-point readout links. The first level uses a limited amount of the total detector information to make a decision in less than 2.5 μs, reducing the rate to about 75 kHz. The two higher levels access more detector information for a final rate of up to 200 Hz with an event size of approximately 1.3 Mbyte.

1.6.1 Trigger system

The L1 trigger searches for high transverse-momentum muons, electrons, photons, jets, and τ-leptons decaying into hadrons, as well as large missing and total transverse energy. Its selection is based on information from a subset of detectors. High transverse-momentum muons are identified using trigger chambers in the barrel and end-cap regions of the spectrometer. Calorimeter selections are based on reduced-granularity information from all the calorimeters. Results from the L1 muon and calorimeter triggers are processed by the central trigger processor, which implements a trigger 'menu' made up of combinations of trigger selections. Pre-scaling of trigger menu items is also available, allowing optimal use of the bandwidth as luminosity and background conditions change. Events passing the L1 trigger selection are transferred to the next stages of the detector-specific electronics and subsequently to the data acquisition via point-to-point links.

In each event, the L1 trigger also defines one or more Regions-of-Interest (RoI's), i.e. the geographical coordinates in η and ϕ, of those regions within the detector where its selection process has identified interesting features. The RoI data include information on the type of feature identified and the criteria passed, e.g. a threshold. This information is subsequently used by the high-level trigger.

2008 JINST 3 S08003

The L2 selection is seeded by the RoI information provided by the L1 trigger over a dedicated data path. L2 selections use, at full granularity and precision, all the available detector data within the RoI's (approximately 2% of the total event data). The L2 menus are designed to reduce the trigger rate to approximately 3.5 kHz, with an event processing time of about 40 ms, averaged over all events. The final stage of the event selection is carried out by the event filter, which reduces the event rate to roughly 200 Hz. Its selections are implemented using offline analysis procedures within an average event processing time of the order of four seconds.

1.6.2 Readout architecture and data acquisition

The Readout Drivers (ROD's) are detector-specific functional elements of the front-end systems, which achieve a higher level of data concentration and multiplexing by gathering information from several front-end data streams. Although each sub-detector uses specific front-end electronics and ROD's, these components are built from standardised blocks and are subject to common requirements. The front-end electronics sub-system includes different functional components:

- the front-end analogue or analogue-to-digital processing;
- the L1 buffer in which the (analogue or digital) information is retained for a time long enough to accommodate the L1 trigger latency;
- the derandomising buffer in which the data corresponding to a L1 trigger accept are stored before being sent to the following level. This element is necessary to accommodate the maximum instantaneous L1 rate without introducing significant deadtime (maximum 1%);
- the dedicated links or buses which are used to transmit the front-end data stream to the next stage.

After an event is accepted by the L1 trigger, the data from the pipe-lines are transferred off the detector to the ROD's. Digitised signals are formatted as raw data prior to being transferred to the DAQ system. The ROD's follow some general ATLAS rules, including the definition of the data format of the event, the error detection/recovery mechanisms to be implemented, and the physical interface for the data transmission to the DAQ system.

The first stage of the DAQ, the readout system, receives and temporarily stores the data in local buffers. It is subsequently solicited by the L2 trigger for the event data associated to RoI's. Those events selected by the L2 trigger are then transferred to the event-building system and subsequently to the event filter for final selection. Events selected by the event filter are moved to permanent storage at the CERN computer centre. In addition to the movement of data, the data acquisition also provides for the configuration, control and monitoring of the hardware and software components which together provide the data-taking functionality.

The DCS permits the coherent and safe operation of the ATLAS detector hardware, and serves as a homogeneous interface to all sub-detectors and to the technical infrastructure of the experiment. It controls, continuously monitors and archives the operational parameters, signals any abnormal behaviour to the operator, and allows automatic or manual corrective actions to be taken. Typical examples are high- and low-voltage systems for detector and electronics, gas and

2008 JINST 3 S08003

cooling systems, magnetic field, temperatures, and humidity. The DCS also enables bi-directional communication with the data acquisition system in order to synchronise the state of the detector with data-taking. It also handles the communication between the sub-detectors and other systems which are controlled independently, such as the LHC accelerator, the CERN technical services, the ATLAS magnets, and the detector safety system.

1.7 Radiation, shielding, and interface to the LHC machine

The experimental conditions at the LHC will be challenging. The unprecedented radiation levels are expected to result in activated detector components and severe beam-induced backgrounds. To mitigate their impact, the ATLAS shielding layout and the LHC beam-pipe design were carefully optimised. Good communication between the LHC and ATLAS operators will be needed during both injection and data-taking, especially to prevent beam-related accidents which could damage the detector.

1.7.1 Radiation levels

At the LHC, the primary source of radiation at full luminosity comes from collisions at the interaction point. In the inner detector, charged hadron secondaries from inelastic proton-proton interactions dominate the radiation backgrounds at small radii while further out other sources, such as neutrons, become more important. Table 1.5 shows projected radiation levels in key areas of the detector (see chapter 3).

In ATLAS, most of the energy from primaries is dumped into two regions: the TAS (Target Absorber Secondaries) collimators protecting LHC quadrupoles and the forward calorimeters. The beam vacuum system spans the length of the detector and in the forward region is a major source of radiation backgrounds. Primary particles from the interaction point strike the beam-pipe at very shallow angles, such that the projected material depth is large. Studies have shown that the beam-line material contributes more than half of the radiation backgrounds in the muon system. The deleterious effects of background radiation fall into a number of general categories: increased background and occupancies, radiation damage and ageing of detector components and electronics, single event upsets and single event damage, and creation of radionuclides which will impact access and maintenance scenarios.

1.7.2 Shielding

In order to limit the effects of radiation on the detector, ATLAS relies on the use of almost 3000 tonnes of shielding (see chapter 3). The shielding procedure is based on a three-layer concept. The inner layer is designed to stop high energy hadrons and secondaries. It is built from materials such as iron or copper which pack a large number of interaction lengths into a limited volume. A second layer, consisting of doped polyethylene rich in hydrogen, is used to moderate the neutron radiation escaping from the first layer; the low energy neutrons are then captured by a boron dopant. Photon radiation is created in the neutron capture process and these photons are stopped in the third shielding layer, which consists of steel or lead.

2008 JINST 3 S08003

Table 1.5: The 1 MeV neutron equivalent fluence (F_{neq}) and doses in key areas of the detector after 500 fb^{-1} of data (estimated to be approximately seven years of operation). Also given are the charged-particle fluxes in the inner detector and fluxes and single-plane rates in the muon spectrometer.

Inner detector					
Location	**F_{neq}** (10^{14} cm^{-2})	**Dose** (kGy)	**Charged-particle flux** above 10 MeV (Hz/cm^2)		
Pixel layer 0	13.5	790	40×10^6		
SCT layer 1	0.8	38	1.5×10^6		
SCT disk 9	0.6	23	10^6		
TRT outer radius	0.25	3.5	10^5		
Calorimeters					
Location	$\lvert\eta\rvert$	**Maximum dose** (kGy)			
EM barrel	1.475	1.2			
EM end-cap	3.2	150			
Tile	1.2	0.15			
HEC	3.2	30			
FCal	4.9	1000			
Muon spectrometer					
Location	**Flux** (kHz/cm^2)		**Flux** (Hz/cm^2)		**Single-plane rates** (Hz/cm^2)
	n	γ	μ	p	
Barrel chambers	2.6–4.0	1.0–1.5	0.3–4.5	0.4–3.2	6.0–11.0
Inner edge of inner wheel	79	25	21	64	347
Inner edge of outer wheel	2.7	1.5	3	0.9	12

1.7.3 Beam-pipe

The 38 m long beam-pipe section in the ATLAS experimental area consists of seven parts, bolted together with flanges to form a fully in-situ bakeable ultra-high vacuum system (see chapter 9). The central chamber is centred around the interaction point and is integrated and installed with the pixel detector. It has a 58 mm inner diameter and is constructed from 0.8 mm thick beryllium. The remaining six chambers, made of stainless steel, are installed symmetrically on both sides of the interaction point. They are supported by the end-cap LAr cryostats, the end-cap toroids and the forward shielding, respectively.

1.7.4 LHC machine interface

The LHC machine and ATLAS must continually exchange information to ensure the safe and optimal operation of the machine (see chapter 9). The LHC machine gives ATLAS such information as beam and bunch intensities, and other characteristics of the beam such as its position. It also provides the 40.08 MHz bunch clock of the accelerator, needed for the L1 trigger and detector

2008 JINST 3 S08003

sub-systems. ATLAS provides information on total luminosity and luminosity per bunch obtained from its luminosity detectors, and indications of the quality of the collisions based on information from the detector and from the beam conditions monitors (see chapter 3). The ATLAS beam interlock system provides information on whether or not to safely inject or dump the beams, or to move from one mode of operation (e.g. filling) to the next (e.g. ramping). This information is exchanged through the detector control system information server, and dedicated hardware links for such critical information as beam permission signals and timing.

1.8 Outline of the paper

This paper is structured as follows. Chapter 2 summarises the key features of the solenoid and toroid magnet system and the B-field determination methodology. The beam-line shielding and the expected radiation levels are presented in chapter 3. This is followed, in chapters 4, 5, and 6, by the description of the inner detector, calorimetry, and muon spectrometer, respectively. The forward detectors, not shown in figure 1.1, are discussed in chapter 7. Chapter 8 outlines the hardware aspects of the trigger and data acquisition systems. Chapter 9 then presents the main features of the infrastructure in the ATLAS cavern, including the overall integration of the experiment, the sub-detector positioning strategy and the corresponding survey results, the services (including cables, pipes, gas and cooling systems, cryogenics, back-up power infrastructure, etc.), the beam-pipe, and the access and maintenance scenarios. Chapter 10 presents an overview of the global performance expected from the ATLAS detector, as obtained from combined test-beam measurements and from the latest analysis results based on the large-scale simulations done for the commissioning of the computing system. Finally, chapter 11 briefly summarises the current status of installation and commissioning, and the expectations for the ultimate completion of the detector and its operation.

2008 JINST 3 S08003